# Fermi surface nesting and intrinsic resistivity of beryllium: First-principles calculations

Zhe Liu, Mingfeng Zhu, and Yisong Zheng*
*Key Laboratory of Physics and Technology for Advanced Batteries (Ministry of Education), Department of Physics, Jilin University, Changchun 130012, People's Republic of China*

(Received 13 April 2019; revised manuscript received 5 June 2019; published 29 July 2019)

Within the semiclassical Boltzmann transport theory, we perform a systematic first-principles calculation of the intrinsic resistivity of beryllium, a nodal-line semimetal. The Wannier interpolation technique to treat the electron-phonon (*e*-ph) interaction is employed to guarantee a high precision of the numerical results. Our numerical results of the intrinsic resistivity of beryllium agree quantitatively with experimental data in a large temperature range. We find that around each joint region between the electron and hole pockets, the Fermi surface of beryllium forms a pair of vertical facets (parallel to *c* axis). Then, the nesting effect between such Fermi surface segments near inequivalent vertices of the hexagonal Brillouin zone can be realized by *e*-ph scattering with a relatively short phonon wavelength. Such a Fermi surface nesting effect plays the dominant role in the intrinsic resistivity. It is also the underlying mechanism for linear temperature dependence of the intrinsic resistivity from a very low critical temperature (200 K). In contrast, the contribution of the topological nontrivial states near the nodal line to the intrinsic resistivity is less important because only a few of such states appear in the vicinity of the Fermi surface due to the sizable dispersion of the nodal line.

DOI: 10.1103/PhysRevB.100.045145

## I. INTRODUCTION

As one of the basic physical properties of metal, the intrinsic resistivity arising from electron-phonon (*e*-ph) scattering has long been an important topic for both theoretical and experimental studies. It is well known that the electric transport ability of metals at room temperature is limited by the intrinsic resistivity since the *e*-ph scattering increases with temperature, dominating over other scattering mechanisms [1]. As a common feature of most metallic materials, its frequently verified by experiments that the intrinsic resistivity $\rho$ is proportional to temperature $T$ at sufficiently high temperature [2–4]. The onset of the linear $\rho$-$T$ relationship is determined by two kinds of characteristic temperatures, i.e., the so-called Debye temperature $T_D$ and Bloch-Grüneisen temperature $T_{BG}$ [5]. According to conventional transport theory, all of the phonons are fully thermally activated above the Debye temperature $T_D$, with the average phonon number being about $T/T_D$. Note that the *e*-ph scattering rate is proportional to the average phonon number. As a result, the linear $\rho$-$T$ relation holds at and beyond Debye temperature. However, for some metallic materials with a very small spherical Fermi surface, it is possible that the linear $\rho$-$T$ relation emerges at a much lower temperature, i.e., $T_{BG}$. This is because the Fermi surface is too small so that at $T_{BG}$, which may be much smaller than $T_D$, the phonons essential for electronic backscattering around the Fermi surface have already been activated thermally.

In general, many semimetals have a much more complicated Fermi surface than a spherical surface, even being composed of both the electronic and hole pockets. With regard to such complicated Fermi surfaces, it is inappropriate to define a Bloch-Grüneisen temperature. Accordingly, these semimetals are expected to have a complicated temperature dependence of the intrinsic resistivity below the Debye temperature, which requires a detailed study of both theoretical and experimental aspects. It was not until the past decade that the *e*-ph interaction in a realistic material could be calculated by means of the density functional perturbation theory [6]. However, it is still a formidable work to perform *ab initio* calculations of the intrinsic resistivity of a metallic material since a fine Brillouin zone sampling is required for calculating *e*-ph scattering around the Fermi surface with high precision. It is indeed an unaffordable computational burden to perform an *e*-ph interaction investigation entirely on the level of the first-principles calculations. Recently, such a difficulty was circumvented by means of the Wannier interpolation technique [7], which paves the way to study the intrinsic resistivity of a realistic metallic material even with a complicated Fermi surface on the level of the first-principles calculations.

The discovery of topological metallic and semimetallic materials [8–13] has reignited interest in studying the intrinsic resistivity of metals, focusing on the influence of the topologically nontrivial band structure on the *e*-ph scattering-limited transport property. Many materials have been discovered as nodal-line topological semimetals (NLSMs) [14–20] in recent years. In particular, alkaline-earth metals such as beryllium were found to be NLSMs [21] and received extensive attention. Although there are a few works involving strong *e*-ph coupling of topological surface states of Be [22] and phase transitions in extreme conditions [23], to our knowledge, a systematic theoretical study on the level of first-principles calculations for the intrinsic resistivity of the bulk material of Be is yet lacking. Thus far, many relevant issues remain unknown, for instance, the effect of the nodal-line state on

*Corresponding author: zys@jlu.edu.cn

 

the intrinsic resistivity, the temperature dependence of the intrinsic resistivity, and the underlying mechanism, as well as the contributions of phonon modes to the intrinsic resistivity of Be.

In this work, we investigate the intrinsic resistivity of the three-dimensional bulk material of Be, a nodal-line semimetal, on the level of first-principles calculations. We find that the Fermi surface of Be consists of electronic and hole pockets with a complicated shape. Near the $K$ and $K'$ points, the electron and hole pockets touch each other, and the Fermi surface therein looks like a pair of facets. The Fermi surface nesting between two pairs of facets near the $K$ and $K'$ points can be realized by the $e$-ph scattering with specified phonon wave vectors. Such $e$-ph scattering processes play the dominant role in contributing to the intrinsic resistivity and determine the linear temperature dependence of the intrinsic resistivity in a large range from 200 to 900 K. In contrast, the topological nontrivial states near the nodal line contribute to the intrinsic resistivity relatively weakly because of the sizable dispersion of the nodal line.

The rest of the present work is organized as follows: In Sec. II, we give a brief description of the theoretical methods, including the technical details of the first-principles calculations and the formulas for calculating the intrinsic resistivity. In Sec. III, numerical results are presented and discussed. Finally, we summarize the main conclusions in Sec. IV.

## II. METHODS AND CONVERGENCES

### A. First-principles calculation

To investigate the intrinsic resistivity of a Be on the level of first-principles calculations, detailed knowledge of the electronic and phononic states and $e$-ph interaction in this material is required. To begin with, we take relatively coarse Brillouin zone (BZ) samplings for the electronic wave vector $\boldsymbol{k}$ and phononic wave vector $\boldsymbol{q}$. It is thus feasible to perform a first-principles calculation on such two coarse meshes for the electronic eigenenergy $E_{n\boldsymbol{k}}$, the phonon frequency $\omega_{\nu\boldsymbol{q}}$, and, more importantly, the scattering matrix elements $g^{\nu}_{nm}(\boldsymbol{k},\boldsymbol{q})$ between an electronic initial state $(n,\boldsymbol{k})$ and a final state $(m,\boldsymbol{k}+\boldsymbol{q})$ by emitting or absorbing a phonon of state $(\nu,\boldsymbol{q})$. Note that $n, m$, and $\nu$ denote the indexes of electron bands and the phonon mode, respectively. The first-principles calculations for the electronic state and phonon state and $e$-ph interaction are performed in the theoretical frameworks of density functional theory (DFT) and density functional perturbation theory (DFPT), respectively, using the QUANTUM ESPRESSO package [24]. In addition, we adopt the norm-conserving pseudopotential [25] to model the ionic potential and the generalized gradient approximation of the Perdew-Burke-Ernzerhof [26] functional for the exchange-correlation interaction. A coarse Monkhorst-Pack [27] $10\times10\times10$ mesh is employed to sample both $k$ points and $q$ points in the first Brillouin zone.

The aforementioned numerical results do not suffice for exploring the intrinsic resistivity of Be quantitatively because the $\boldsymbol{k}$ mesh and $\boldsymbol{q}$ mesh are both too coarse to result in an accurate description of the $e$-ph scattering processes in the proximity of the Fermi surface. However, first-principles calculations on a much finer $\boldsymbol{k}$ mesh or $\boldsymbol{q}$ mesh imply a formidable computational burden. To circumvent such a prohibitive task, we adopt a generalized Fourier interpolation approach realized by the EPW code [28] in real space, which enables affordable and accurate calculations of the electronic and phonon energy spectra as well as the $e$-ph coupling on ultrafine $500\times500\times500$ $\boldsymbol{k}$-point sampling and $50\times50\times50$ $\boldsymbol{q}$-point sampling. The Dirac $\delta$ function is approximated by the Gaussian smearing function, with a width $\sigma = 0.001$ eV.

### B. Ziman's resistivity formula

Finally, with regard to the calculation of the intrinsic resistivity of Be we employ Ziman's resistivity formula [29], which we outline as follows. By virtue of a variational method for solving the Boltzmann transport equation with the $e$-ph interaction as the scattering mechanism for electronic transport, the intrinsic resistivity of the metal can be formulated in terms of the Eliashberg transport coupling function. It is the so-called Ziman resistivity formula which expresses the longitudinal resistivity along a given direction, say, the $x$ direction, in the form

$$\rho_x = \frac{\pi}{e^2\hbar N_{E_f}\langle v_x^2\rangle}\int d\Omega\alpha^2_{tr}F(\Omega)\mathcal{F}\left(\frac{k_BT}{\Omega}\right), \tag{1}$$

where

$$\mathcal{F}\left(\frac{k_BT}{\Omega}\right) = \frac{\Omega}{k_BT}\sinh^{-2}\left(\frac{\Omega}{2k_BT}\right). \tag{2}$$

$N_{E_f}$ stands for the electronic density of states at the Fermi energy $E_f$; $T$ is temperature, and $\langle v_x^2\rangle$ denotes a squared average of the $x$ component of electronic velocity on the Fermi surface, that is,

$$\langle v_x^2\rangle = \frac{\sum_{n\boldsymbol{k}}[(\boldsymbol{v}_{n\boldsymbol{k}})_x]^2\delta(E_{n\boldsymbol{k}}-E_f)}{\sum_{n\boldsymbol{k}}\delta(E_{n\boldsymbol{k}}-E_f)}, \tag{3}$$

with $\boldsymbol{v}_{n\boldsymbol{k}} = \nabla E_{n\boldsymbol{k}}/\hbar$ being the electronic group velocity. The Eliashberg transport coupling function is defined as

$$\alpha^2_{tr}F(\Omega) = \sum_{\boldsymbol{q}\nu}\omega_{\boldsymbol{q}\nu}\lambda_{tr,\boldsymbol{q}\nu}\delta(\Omega-\hbar\omega_{\boldsymbol{q}\nu}), \tag{4}$$

with

$$\lambda_{tr,\boldsymbol{q}\nu} = \frac{1}{N_{E_f}\omega^2_{\boldsymbol{q}\nu}}\sum_{mn\boldsymbol{k}}\left|\mathcal{G}^{\nu}_{mn}(\boldsymbol{k},\boldsymbol{q})\right|^2\delta(E_{m\boldsymbol{k}+\boldsymbol{q}}-E_{n\boldsymbol{k}}-\hbar\omega_{\boldsymbol{q}\nu}) \times\left(f^0_{n\boldsymbol{k}}-f^0_{m\boldsymbol{k}+\boldsymbol{q}}\right)\left[1-\frac{\boldsymbol{v}_{n\boldsymbol{k}}\cdot\boldsymbol{v}_{m\boldsymbol{k}+\boldsymbol{q}}}{|\boldsymbol{v}_{n\boldsymbol{k}}|^2}\right], \tag{5}$$

where $f^0_{n\boldsymbol{k}}$ and $f^0_{m\boldsymbol{k}+\boldsymbol{q}}$ denote the Fermi-Dirac distributions at the respective electronic states. Substituting Eqs. (2)–(4) into Eq. (1) and integrating out $\Omega$, the intrinsic resistivity can be expressed as

$$\rho_x = \sum_{nm\boldsymbol{k}}\sum_{\boldsymbol{q}\nu}\rho^{\nu}_{nm}(\boldsymbol{k},\boldsymbol{q}), \tag{6}$$

where

$$\rho^{\nu}_{nm}(\boldsymbol{k},\boldsymbol{q}) = \frac{\pi\beta}{e^2\hbar N^2_{E_f}\langle v_x^2\rangle}\sinh^{-2}\left(\frac{\omega_{\boldsymbol{q}\nu}}{2k_BT}\right)\left|\mathcal{G}^{\nu}_{mn}(\boldsymbol{k},\boldsymbol{q})\right|^2 \times \delta(E_{n\boldsymbol{k}} - E_{m\boldsymbol{k}+\boldsymbol{q}} - \omega_{\boldsymbol{q}\nu})(f^0_{n\boldsymbol{k}} - f^0_{m\boldsymbol{k}+\boldsymbol{q}}) \times \left(1 - \frac{\boldsymbol{v}_{n\boldsymbol{k}}\cdot\boldsymbol{v}_{m\boldsymbol{k}+\boldsymbol{q}}}{|\boldsymbol{v}_{n\boldsymbol{k}}|^2}\right) \quad (7)$$

stands for the contribution of one individual scattering procedure to the intrinsic resistivity. We can also define

$$\rho(\boldsymbol{k}) = \sum_{nm\boldsymbol{q}\nu}\rho^{\nu}_{nm}(\boldsymbol{k},\boldsymbol{q}), \quad (8)$$

which represents the contribution of a specific electronic wave vector $\boldsymbol{k}$ to the intrinsic resistivity. Furthermore, we define

$$\rho_x = \sum_{\boldsymbol{q}\nu}\rho^{\nu}(\boldsymbol{q}), \quad (9)$$

where

$$\rho^{\nu}(\boldsymbol{q}) = \sum_{nm\boldsymbol{k}}\rho^{\nu}_{nm}(\boldsymbol{k},\boldsymbol{q}) \quad (10)$$

and

$$\rho(\boldsymbol{q}) = \sum_{\nu}\rho^{\nu}(\boldsymbol{q}). \quad (11)$$

Here $\rho^{\nu}(\boldsymbol{q})$ and $\rho(\boldsymbol{q})$ show the individual contribution of each phonon state and phonon wave vector $\boldsymbol{q}$, respectively.

## III. RESULTS AND DISCUSSION

With the theoretical approaches presented above, we are in the position to perform numerical calculations on the intrinsic resistivity of Be. Before proceeding, it is significant to have a look at the crystal structure and electron and phonon dispersions of Be. Be has a hexagonal crystal structure, with symmetry characterized by the space group $P6_3/mmc$. The unit cell and the Brillouin zone of Be are shown in Fig. 1. After a full optimization, the lattice parameters of Be are found to be $\boldsymbol{a}_1 = 2.24$ Å and $\boldsymbol{a}_3 = 3.55$ Å, which indicates the appreciable anisotropy of the crystal structure. And such anisotropy will manifest itself in the intrinsic resistivity shown below. The electronic band structures of Be along the high-symmetry lines are exhibited in Fig. 2(a), from which we can see that more than one band spans the Fermi level. Hence, Be has a complicated Fermi surface, which will be detailed later on. As reported in the previous work [21], Be is a topological nodal-line semimetal since there exists an almost circular nodal line around the BZ center. The energy dispersion of the nodal line ranges from 0 to 1.1 eV with respect to the Fermi level, and the energy minimal and maximal points of the nodal line occur along the high-symmetry lines Γ-$M$ and Γ-$K$, respectively, as labeled by $N_1$ and $N_2$ in Fig. 2(a). Note that the nodal point $N_2$ is higher than the Fermi level by about 1.1 eV; it is too high to contribute to the intrinsic resistivity even at room temperature since it hardly takes part in the $e$-ph scattering process around the Fermi surface. Phonon dispersion with no imaginary frequency is presented in Fig. 2(b), where the phonon modes are identified from $\nu = 1$ to 6 ordered by frequency. Of course, around the Γ point the two nearly degenerate lowest-frequency modes are transverse-acoustic (TA) modes. In addition, the calculated maximal phonon frequency is about 75 meV, still much too low to excite an electron at the Fermi surface to the nodal point $N_2$.

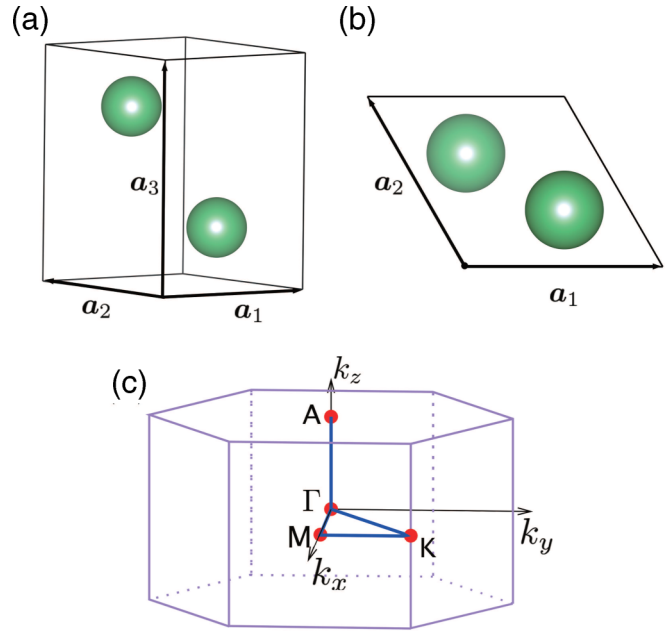


FIG. 1. (a) and (b) The unit cell of the Be lattice. (c) Brillouin zone of Be with high-symmetry points labeled.

The three-dimensional Fermi surface and a two-dimensional view of it with $k_z$ scaled by color are displayed in Figs. 3(a) and 3(b), respectively. The Fermi surface consists of two separate electronic pockets centered at the $K$ and $K'$ points, respectively, as well as one connected hole pocket inside of the BZ. In contrast to the hole pocket, the two electronic pockets have a much larger extension in the $k_z$ direction. We can see an extreme case at the part of the hole pocket closest to Γ, i.e., a circle at $k_z = 0$, with no extension in the $k_z$ direction. As a result, the nodal-line states at this circle are much fewer than the states near the junction of the pockets, which could suppress the contribution of Dirac nodal line states to resistivity. In addition, it should be noted that around each juncture region between the electron and hole pockets the Fermi surface forms a pair of facets which, as seen below, plays the critical role in contributing to the intrinsic resistivity due to the Fermi surface nesting effect.

With the help of the EPW interpolation technique, in order to calculate the intrinsic resistivity with high precision, we can employ very fine BZ samplings to treat the $\boldsymbol{k}$ and $\boldsymbol{q}$ integrations numerically. As shown in Figs. 4(a)–4(c), we find that at room temperature (300 K), a $500 \times 500 \times 500$ $k$ mesh and a $50 \times 50 \times 50$ $q$ mesh with an appropriate Gaussian broadening $\sigma = 0.001$ eV can bring us convergent results of the intrinsic resistivity. In comparison with the result obtained with much finer $k$ and $q$ meshes, the relative error of the obtained intrinsic resistivity is less than 2%. In addition, even at very low temperature our numerical calculations indicate such fine $k$ and $q$ meshes are sufficient to result in a convergent

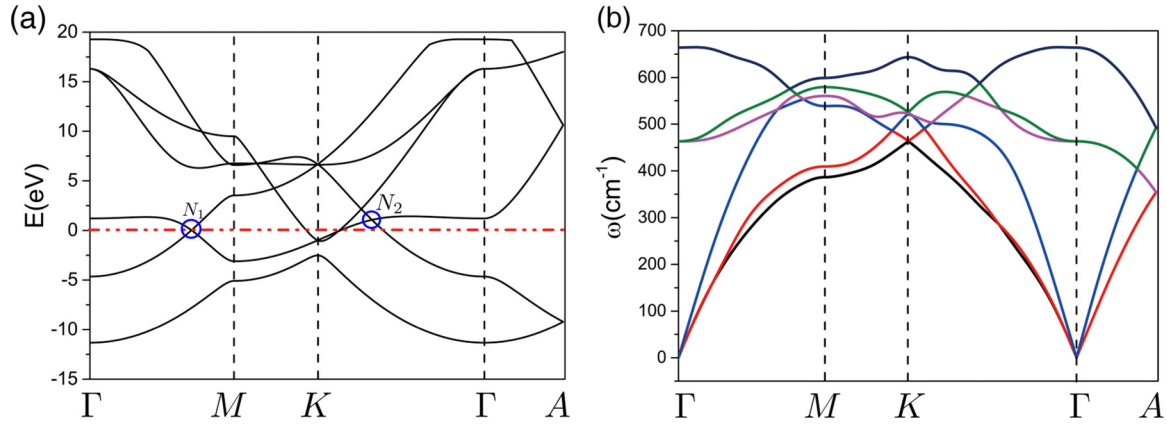


FIG. 2. (a) Electronic and (b) phononic dispersions of Be along the high-symmetry path. Fermi energy is shifted to be 0 eV, and nodal-line states ($N_1$ and $N_2$) are marked with blue circles. The phonon modes are identified by magnitude from 1 (the lowest) to 6 (the highest).

result of the intrinsic resistivity with a relative error less than 5%.

In Fig. 5(a), our calculated results of the resistivities along the $x$ and $z$ directions as functions of temperature are compared with an experimental result by Mitchell [30]. In general, our results agree with the experimental ones in the whole temperature range. Owing to the anisotropy of the crystal structure as shown in Fig. 1, the intrinsic resistivity of Be shows notable anisotropy. The anisotropy ratio, defined as $\rho_z/\rho_x$, is about 1.5 in our numerical result, and it is independent of temperature. In the experimental work, it ranges from 1.0 to 1.4 when temperature varies from 150 to 300 K and stays nearly unchanged when $T$ goes higher. In Fig. 5(b) our numerical result for the intrinsic resistivity of polycrystalline Be, defined as $\rho_{\text{poly}} = (2\rho_x + \rho_z)/3$, is compared with the experimental result, as well as another theoretical result with single-site approximation [31] and some approximate models by Sano [32]. One can see that in contrast to Sano's result, our numerical result agrees better with the experimental result in almost the whole temperature range. What we would like to emphasize is that all the theoretical results for the intrinsic resistivity (ours and Sano's) show a linear temperature dependence as long as the temperature is higher than 200 K, which is far lower than the Debye temperature of Be (900 K). Moreover, it seems also unreasonable to define a Bloch-Grüneisen temperature to account for the linear $\rho$-$T$ relation with a low onset temperature since Be has a complicated Fermi surface. In contrast, as shown in Fig. 5, the experimental result does not show unambiguously a linear temperature dependence in the whole temperature range. The possible reasons for the discrepancy between the theoretical and experimental results may be the quantum nuclear effect of Be excluded by the Born-Oppenheimer approximation and other scattering mechanisms influencing the experimental result.

In order to understand the low onset temperature for the linear temperature dependence of the intrinsic resistivity obtained by our numerical calculation, it is necessary to analyze in depth the ingredients of the intrinsic resistivity. To begin with, let us to look at contributions of individual $\boldsymbol{k}$ points to $\rho_x$ (hereafter, we drop the subscript for simplicity), i.e., $\rho(\boldsymbol{k})$ defined by Eq. (7). The numerical results are displayed in Fig. 6. At a low temperature, say, 50 K, as shown in Fig. 6(a), the $\boldsymbol{k}$ points with large contributions to intrinsic resistivity spread all over the Fermi surface uniformly. That is to say, on the Fermi surface no $\boldsymbol{k}$ point dominates over others to contribute to the intrinsic resistivity at such a low

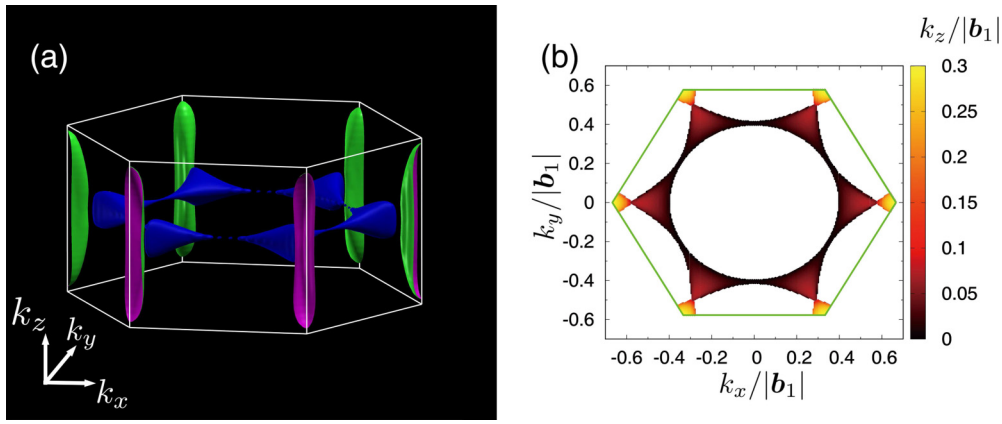


FIG. 3. Fermi surface of Be in (a) the 3D view and (b) the 2D view with $k_z$ marked by colors. In (b), $k_\alpha(\alpha = x, y, z)$ is in units of the reciprocal lattice vector $\boldsymbol{b}_1$, and the edge of the BZ is plotted as a green solid line. Two electron pockets are at $K$ and $K'$, and another pocket [blue in (a)] is a hole pocket.

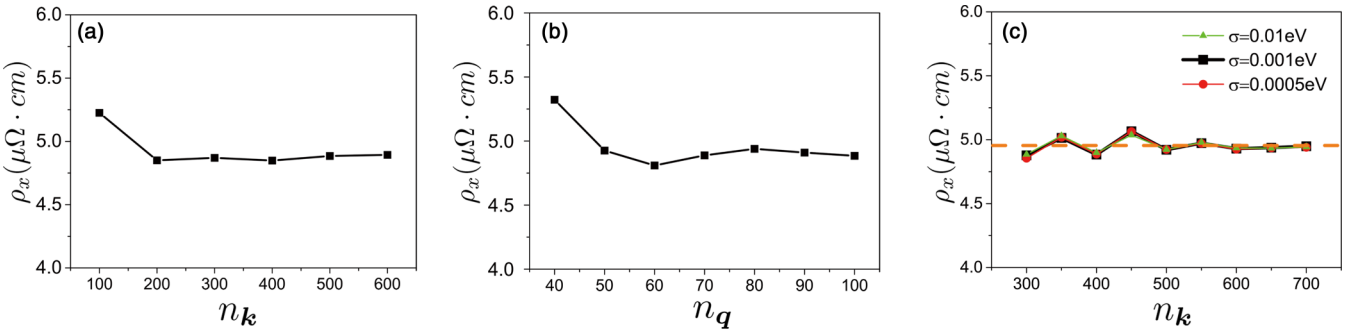


FIG. 4. (a) Convergence of the resistivity with a varied $n_k \times n_k \times n_k$ $\boldsymbol{k}$ mesh and a fixed $100 \times 100 \times 100$ $\boldsymbol{q}$ mesh. (b) Convergence of the resistivity with a fixed $600 \times 600 \times 600$ $\boldsymbol{k}$ mesh and a varied $n_q \times n_q \times n_q$ $\boldsymbol{q}$ mesh. (c) Resistivity with varied Gaussian spreading $\sigma$ and an $n_k \times n_k \times n_k$ $\boldsymbol{k}$ mesh, with a fixed $50 \times 50 \times 50$ $\boldsymbol{q}$ mesh; the orange dashed line is the resistivity by the tetrahedron method. All results are calculated at 300 K.

temperature. This is because the temperature is too low to excite all of the phonons, so the electron states near the Fermi surface can only be scattered by limited long-wave acoustic phonons to their adjacent states. When $T$ is raised to 200 K, as shown in Fig. 6(b), some points on the Fermi surface become more important, especially those around the juncture regions between the electronic and hole pockets. These $\boldsymbol{k}$ points contribute to the intrinsic resistivity by at least 70%. In contrast, the contribution of the $k$ points around the crossing point between the nodal line and the Fermi surface is less than 10%. At first, only a small number of $k$ points around the nodal line fill in the energy window for $e$-ph scattering around the Fermi surface because of the nontrivial energy dispersion of the nodal line. In addition, even for those nodal-line states around the Fermi surface, their contributions to the intrinsic resistivity are not expected to be nontrivial because backscattering between nodal-line states is forbidden since it requires a flip of the pseudospin. Therefore, our numerical result with regard to the unimportance of nodal-line states to the intrinsic resistivity may be viewed as an indirect proof of the backscattering lacking for nodal-line fermions. With temperatures higher than 200 K [Figs. 6(c)–6(e)], the difference between high-contribution points and other points is much more clear.

The length of the phononic wave vector, i.e., $|\boldsymbol{q}|$-resolved resistivity

$$\rho_{|\boldsymbol{q}|} = \sum_{\boldsymbol{q}'\nu} \rho^{\nu}_{\boldsymbol{q}'} \delta(|\boldsymbol{q}| - |\boldsymbol{q}'|), \tag{12}$$

is plotted in Figs. 7(a)–7(e), and we find interesting results here. At low temperature, say, 50 K, the resistivity is dominated by long-wave phonons, unsurprisingly. However, when $T$ goes a little higher to 100 K, another peak with a much larger length of the wave vector $q_0 = \frac{1.2\pi}{|a_1|}$ emerges beyond expectation. If temperature increases to 200 K or higher, even as high as 500 K, the long-wave phonons show very little impact on resistivity and the peak with $|\boldsymbol{q}| = q_0$ becomes higher, which indicates astonishing dominating roles of these phonons. Although fewer phonons with $|\boldsymbol{q}| = q_0$ are excited than the long-wave phonon, these short-wave phonons still contribute most of the resistivity. We also calculate the

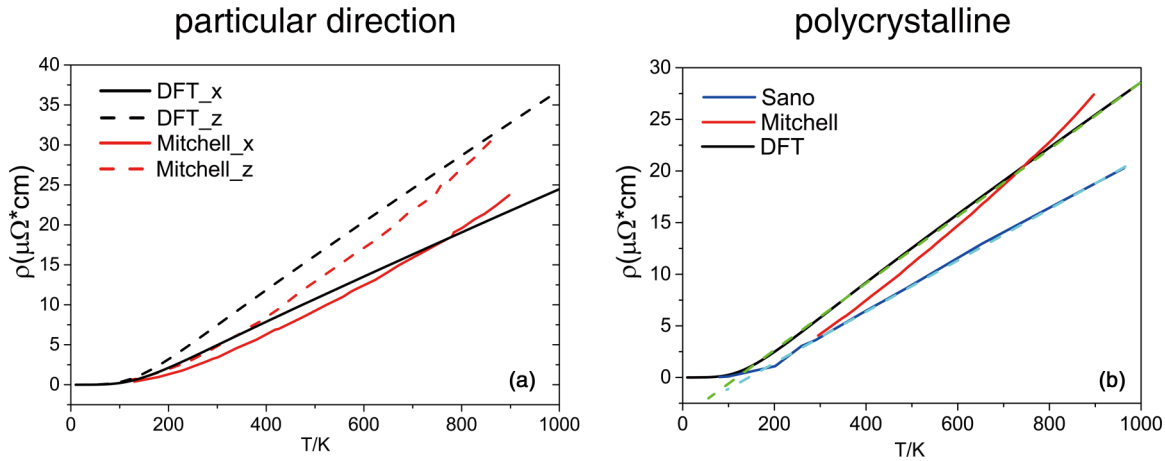


FIG. 5. (a) Resistivity of Be versus temperature $T$ in the $x$ and $z$ directions calculated in this work (named DFT, in black) is compared with an experimental result by Mitchell (in red). (b) Resistivity of Be of polycrystal ($\rho_{\text{poly}} = (2\rho_x + \rho_z)/3$) by us(in black) is compared with an experimental result by Mitchell [30] (in red) and a semiempirical result by Sano [32] (in blue). $\rho_{\text{poly}}$ calculated by us is closer to the experimental result than Sano's work in the case of $T > 450$ K. Both our and Sano's theoretical results give the linear $\rho$-$T$ relationship as $T > 200$ K.

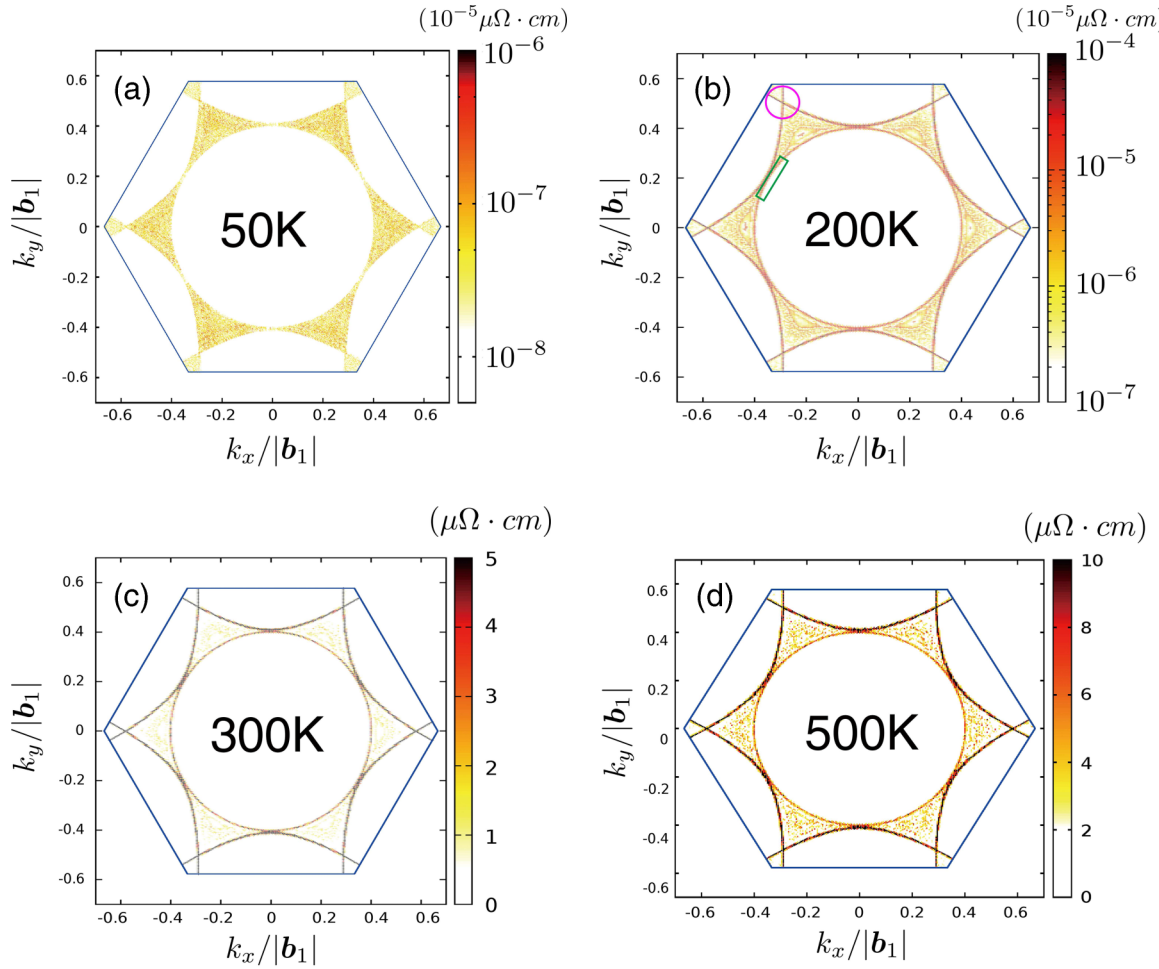


FIG. 6. The $\boldsymbol{k}$-resolved resistivity $\rho(\boldsymbol{k})$ at different temperatures. The edges of the BZ are plotted by a blue solid line. One of the junctures of the electron and hole pockets is indicated with a fuchsia circle, and the nodal-line states near $E_f$ are indicated with a green rectangle in (b). Due to the $C_6$ symmetry, there are five other junctures between the electron and hole pockets.

contribution of each mode to $|\boldsymbol{q}|$-resolved resistivity

$$\rho^{\nu}_{|\boldsymbol{q}|} = \sum_{\boldsymbol{q}'} \rho^{\nu}_{\boldsymbol{q}'} \delta(|\boldsymbol{q}| - |\boldsymbol{q}'|) \tag{13}$$

at 300 K and plot it in Fig. 7(f). Like for $\rho_{|\boldsymbol{q}|}$, all modes show the same peak at $\boldsymbol{q}_0$, but the lowest TA mode is the most important. The relative contributions of the modes from 1 to 6 to the resistivity are calculated as 30.6%, 14.2%, 18.6%, 11.4%, 12.4%, and 12.8%, respectively. These facts suggest that there must be a peculiar scattering mechanism in Be.

To combine the numerical results shown in Figs. 6 and 7 and to calculate $\rho^{\nu}_{nm}(\boldsymbol{k}, \boldsymbol{q})$ as defined by Eq. (6) to identify the contributions of individual $e$-ph scattering processes to the intrinsic resistivity, we find that Be has a special Fermi surface nesting effect which plays the dominant role in contributing to the intrinsic resistivity. Such a Fermi surface nesting is illustrated in Fig. 8. As mentioned above, the Fermi surface of Be looks like two vertical facets around the juncture regions between the electronic and hole pockets. As shown in Fig. 8(a), two such facets near the $K$ point are denoted as $A_1$ and $A_2$, and another two near the $K'$ point labeled $B_1$ and $B_2$ are parallel to the former two, i.e., $A_1 \parallel B_1$ and $A_2 \parallel B_2$. Consequently, as shown in Fig. 8(a), Fermi surface nesting can be realized between such two pairs of facets by umklapp $e$-ph scattering processes, where the equation $\boldsymbol{k}' = \boldsymbol{k} + \boldsymbol{q} + \boldsymbol{G}$ is satisfied with a nonzero reciprocal lattice $\boldsymbol{G}$. Generally speaking, the umklapp process is considered to be one of the important scattering mechanisms for the intrinsic resistivity, as it usually leads to a large-angle scattering, resulting in a large variation of electronic velocity [33]. In particular, the umklapp process is the key role in breaking the "Bloch $T^5$ law" of the intrinsic resistivity of most metallic materials at low temperature [34–36]. As seen below, the nature of the large-angle scattering of the umklapp process is one of the reasons for the Fermi surface nesting being the dominant role in determining the intrinsic resistivity of Be. The nesting wave vector $\boldsymbol{q}_0$ connecting the facets has a length of just $\frac{1.2\pi}{|a_1|}$. Due to the $C_3$ rotational symmetry, similar nesting effects can occur between two other pairs of Fermi surfaces, as shown in Fig. 8(b). Notice that the length of the nesting wave vectors which have different directions is the same for these different Fermi surface nestings, i.e., $q_0 = \frac{1.2\pi}{|a_1|}$. In addition, owing to the space inversion symmetry, the electronic states on facets $A_1$ and $B_1$ (and also $A_2$ and $B_2$) have opposite velocities. As a result, the Fermi surface nesting always corresponds to the large-angle scattering, which implies the large

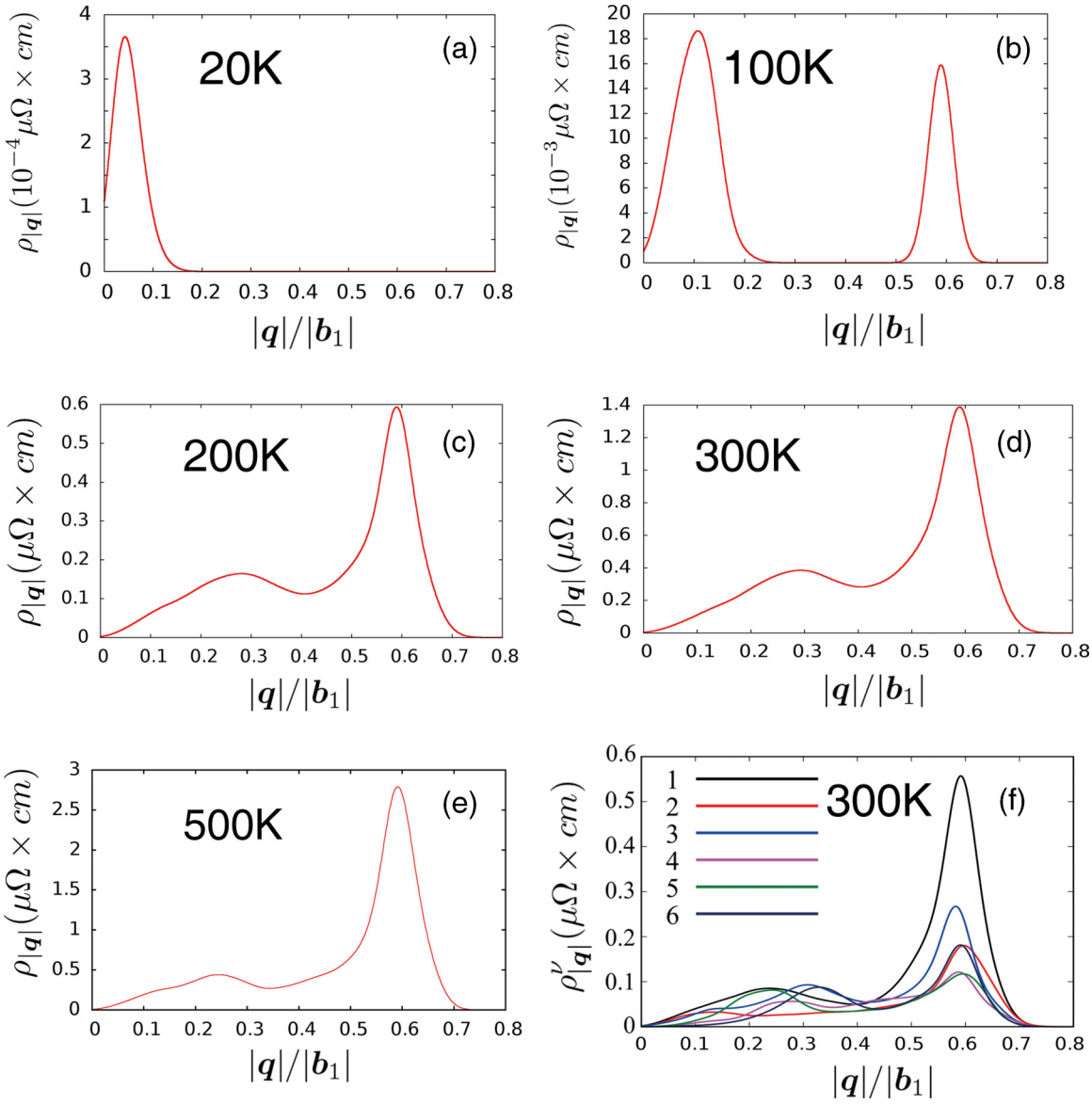


FIG. 7. (a)–(e) The $|\boldsymbol{q}|$-resolved resistivity $\rho_{|\boldsymbol{q}|}$ at different temperatures. The peaks in (b), (c), and (d) are at $0.59|\boldsymbol{b}_1|$, which coincides with $|\boldsymbol{q}_0|$. (f) $|\boldsymbol{q}|$ and mode-resolved resistivity at 300 K; all peaks are at $|\boldsymbol{q}_0|$ too.

weighting contributions to the intrinsic resistivity. In contrast, the long-wave acoustic phonon can only scatter an electron to adjacent states, which is scarcely a large-angle scattering process. Therefore, it is surprising that as shown in Fig. 7, at a relatively low temperature, e.g., 200 K, the Fermi surface nesting effect becomes more important than the long-wave phonon scattering in contributing to the intrinsic resistivity.

Now we are ready to give a reasonable explanation for the untimely occurrence of the linear temperature dependence of the theoretical result of the intrinsic resistivity of Be. According to Eq. (1), the temperature dependence of the intrinsic resistivity arises from both the transport spectral function $\alpha^2_{tr}F(\Omega)$ and the function $\mathcal{F}(k_BT/\Omega)$. They arise from the temperature dependence of the electron and phonon distributions and are plotted in Figs. 9(a) and 9(b), respectively. The function $\mathcal{F}(k_BT/\Omega)$ says that the linear $\rho$-$T$ relation occurs with an onset temperature of $0.22T_D$ [see Fig. 9(b)]. $T_D$ is a cutoff frequency (in units of temperature) beyond which the transport spectrum function vanishes rapidly. $T_D$ is determined by the Debye frequency or the Bloch-Grüneisen temperature in the case of a small Fermi surface (for the case of Be, $T_D \approx 900$ K). However, the $\rho$-$T$ relation is also influenced by the $e$-ph transport spectrum function. We find that owing to the Fermi surface nesting, $\alpha^2_{tr}F(\Omega)$ is independent of temperature as $T > 200$ K. As shown in Eq. (5), at the nesting vector $q_0$ the joint density of states $\delta[E_{nk} - E_{mk+q_0} - \omega_{q_0\nu}]$ is singular when the two electronic states are in the nesting facets where $\nabla[E_{nk} - E_{mk+q_0}] = 0$. This implies that the electronic states around the nesting facets make the dominant contribution to the transport spectral function. In addition, the difference between the two Fermi distribution functions in Eq. (5) gives a $\delta$-function-like peak around Fermi energy with temperature broadening. When $T > 200$, the temperature broadening is large enough to incorporate all the Fermi surface nesting processes into the $k$ summation in Eq. (5). Therefore, $\alpha^2_{tr}F(\Omega)$ becomes temperature independent. This implies that as

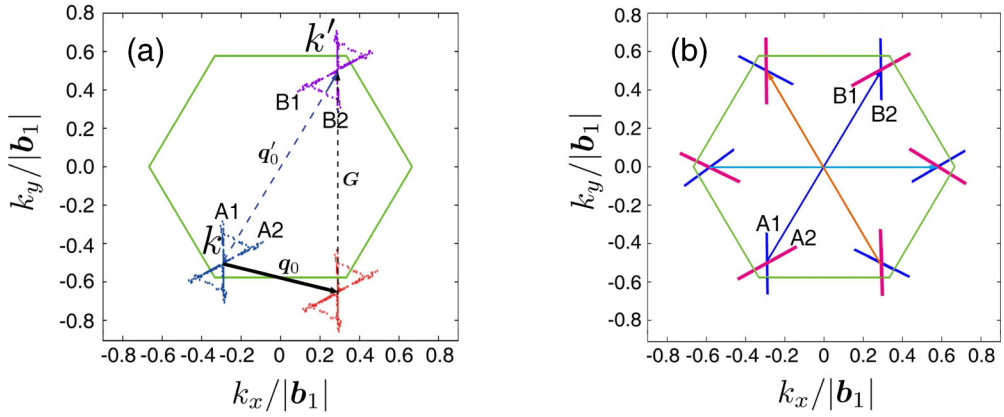


FIG. 8. (a) Top view of two pairs of vertical facets crossing at the $k$ and $k'$ points, both of which are the Fermi surface segments around the joint regions between electronic and hole pockets. Fermi surface nesting between the two segments can be realized by $e$-ph scattering via an umklapp process of $\boldsymbol{k}' = \boldsymbol{k} + \boldsymbol{q}_0 + \boldsymbol{G}$, where $\boldsymbol{q}_0$ and $\boldsymbol{G}$ are the phonon vector and lattice reciprocal vector, respectively. (b) A simple illustration of all the possible Fermi surface nestings between the vertical facets near the inequivalent vertices of the Brillouin zone. Note that any facet is parallel to its nesting partner, e.g., $A_1 \parallel B_1, A_2 \parallel B_2$.

$T > 200$ K, the temperature dependence of resistivity is solely determined by the function $\mathcal{F}(k_BT/\Omega)$, which gives a linear $\rho$-$T$ relation with an onset temperature $T \approx 0.22T_D \approx 200$ K.

In the relevant literature the $e$-ph transport spectrum function is often suggested to take the form of a double-$\delta$ approximation. In such an approximation the temperature dependence of the transport spectrum function is completely omitted. As a result, the temperature dependence of the resistivity is solely determined by the function $\mathcal{F}(k_BT/\Omega)$. Our work indicates that the temperature dependence of the transport spectrum function is associated with the details of the Fermi surface, which influences the $\rho$-$T$ relation to some extent. A noteworthy issue is whether it is suitable to adopt the double-$\delta$ approximation to calculate the $e$-ph transport spectrum function for metallic materials, especially for those with a complicated Fermi surface. Such a topic is left for future study.

## IV. CONCLUSIONS

In this work, we have performed a systematic theoretical study of the intrinsic resistivity of bulk Be, a nodal-line topological semimetal, by means of the first-principles calculations along with the Wannier interpolation method. The calculated resistivities $\rho_x$ and $\rho_z$, i.e., the ones perpendicular and parallel to the $c$ axis, respectively, agree quantitatively with an experimental result and a previous semiempirical theoretical result in a large temperature range from 50 to 900 K. We have found that the intrinsic resistivity shows anisotropy, with the ratio $\rho_z/\rho_x$ being about 1.5, independent of temperature. This result also agrees with the experimental value (1.4 at 300 K or higher). More interestingly, our calculation has shown that the intrinsic resistivity of Be begins to depend on temperature linearly just above a critical temperature, i.e., $T_c = 200$ K, which coincides with the previous theoretical result. Such a critical temperature (200 K) is much smaller than the Debye temperature of Be (900 K). In addition, the complicated Fermi surface prevents us from defining a Bloch-Grüneisen temperature. Hence, Bloch-Grüneisen theory is not applicable to explain such a low critical temperature for the linear temperature dependence of the intrinsic resistivity of Be.

With such a problem, we studied in depth the profile of the Fermi surface and the individual contributions of electronic

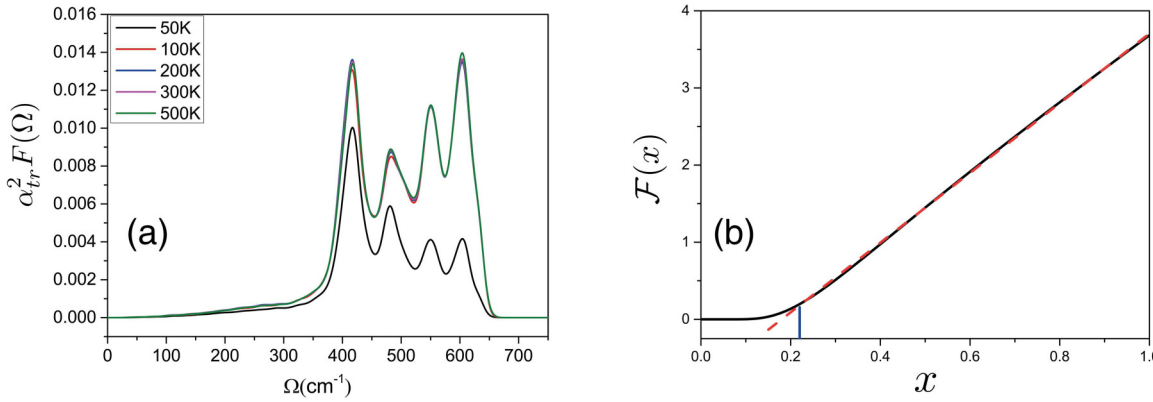


FIG. 9. (a) The Eliashberg transport coupling function at different temperatures. (b) The plot of the function $\mathcal{F}(x)$ (black solid line). When the argument $x < 0.22$, the function $\mathcal{F}(x)$ begins to deviate from a linear function (red dashed line).

and phonon states to the intrinsic resistivity. We found that the electron and hole pockets of the Fermi surface touch each other near the six vertices of the hexagonal Brillouin zone, i.e., the $K$ and $K'$ points. Around such touching regions, the Fermi surface looks like a pair of vertical facets (parallel to the $c$ axis). And any pair of facets near the $K$ point has a counterpart parallel to it farthest $K'$ point. Hence, the Fermi surface nesting can be realized between them by $e$-ph scattering processes with a specific phonon wave vector. With the increase of temperature, the $e$-ph scattering processes associated with the Fermi surface nesting become the dominant feature in limiting the intrinsic resistivity. Although all phonon modes with a nesting wave vector take part in the Fermi surface nesting, the acoustic transverse phonon mode is the most important one. Our numerical result indicates that as the temperature gets higher than 200 K, the Eliashberg transport spectral function is independent of temperature, owing to the Fermi surface nesting effect. Accordingly, the linear temperature dependence of the intrinsic resistivity of Be with a very low critical temperature (200 K) can be well justified. In contrast to the Fermi surface nesting effect, the contribution of the topological nontrivial states near the nodal line to the intrinsic resistivity of Be is less important because only a few such states appear in the vicinity of the Fermi surface due to the sizable dispersion of the nodal line.

## ACKNOWLEDGMENTS

This work was financially supported by the National Natural Science Foundation of China (Grants No. 11474122 and No. 11774123), the National Science Foundation for Young Scientists of China (Grants No. 11404132, No. 11504125, and No. 11504319), and the the Natural Science Foundation of Jilin Province of China (Grant No. 20190201123jc). We thank the High Performance Computing Center of Jilin University for their calculation resources.

[1] J. Bardeen and D. Pines, Phys. Rev. **99**, 1140 (1955).
[2] A. H. Wilson, *The Theory of Metals*, 2nd ed. (Cambridge University Press, Cambridge, 1954).
[3] N. Bäcklund, J. Phys. Chem. Solids **20**, 1 (1961).
[4] D. B. Tanner and D. C. Larson, Phys. Rev. **166**, 652 (1968).
[5] J. M. Ziman, *Principles of the Theory of Solids*, 2nd ed. (Cambridge University Press, Cambridge, 1972).
[6] S. Baroni, S. De Gironcoli, A. Dal Corso, and P. Giannozzi, Rev. Mod. Phys. **73**, 515 (2001).
[7] F. Giustino, M. L. Cohen, and S. G. Louie, Phys. Rev. B **76**, 165108 (2007).
[8] S. M. Young, S. Zaheer, J. C. Y. Teo, C. L. Kane, E. J. Mele, and A. M. Rappe, Phys. Rev. Lett. **108**, 140405 (2012).
[9] Z. K. Liu, B. Zhou, Y. Zhang, Z. J. Wang, H. M. Weng, D. Prabhakaran, S.-K. Mo, Z. X. Shen, Z. Fang, X. Dai, Z. Hussain, and Y. L. Chen, Science **343**, 864 (2014).
[10] X. Wan, A. M. Turner, A. Vishwanath, and S. Y. Savrasov, Phys. Rev. B **83**, 205101 (2011).
[11] S.-Y. Xu, I. Belopolski, N. Alidoust, M. Neupane, G. Bian, C. Zhang, R. Sankar, G. Chang, Z. Yuan, C.-C. Lee, S.-M. Huang, H. Zheng, J. Ma, D. S. Sanchez, B. Wang, A. Bansil, F. Chou, P. P. Shibayev, H. Lin, S. Jia, and M. Z. Hasan, Science **349**, 613 (2015).
[12] C. Fang, Y. Chen, H.-Y. Kee, and L. Fu, Phys. Rev. B **92**, 081201(R) (2015).
[13] A. A. Burkov, M. D. Hook, and L. Balents, Phys. Rev. B **84**, 235126 (2011).
[14] C. Niu, P. M. Buhl, G. Bihlmayer, D. Wortmann, Y. Dai, S. Blügel, and Y. Mokrousov, Phys. Rev. B **95**, 235138 (2017).
[15] H. Weng, Y. Liang, Q. Xu, R. Yu, Z. Fang, X. Dai, and Y. Kawazoe, Phys. Rev. B **92**, 045108 (2015).
[16] S. Murakami, M. Hirayama, R. Okugawa, and T. Miyake, Sci. Adv. **3**, e1602680 (2017).
[17] Y. Chen, Y. Xie, S. A. Yang, H. Pan, F. Zhang, M. L. Cohen, and S. Zhang, Nano Lett. **15**, 6974 (2015).
[18] Y. Kim, B. J. Wieder, C. L. Kane, and A. M. Rappe, Phys. Rev. Lett. **115**, 036806 (2015).
[19] R. Yu, H. Weng, Z. Fang, X. Dai, and X. Hu, Phys. Rev. Lett. **115**, 036807 (2015).
[20] K. Mullen, B. Uchoa, and D. T. Glatzhofer, Phys. Rev. Lett. **115**, 026403 (2015).
[21] R. Li, H. Ma, X. Cheng, S. Wang, D. Li, Z. Zhang, Y. Li, and X.-Q. Chen, Phys. Rev. Lett. **117**, 096401 (2016).
[22] T. Y. Chien, X. He, S.-K. Mo, M. Hashimoto, Z. Hussain, Z.-X. Shen, and E. W. Plummer, Phys. Rev. B **92**, 075133 (2015).
[23] J.-W. Xian, J. Yan, H.-F. Liu, T. Sun, G.-M. Zhang, X.-Y. Gao, and H.-F. Song, Phys. Rev. B **99**, 064102 (2019).
[24] P. Giannozzi, O. Andreussi, T. Brumme, O. Bunau, M. B. Nardelli, M. Calandra, R. Car, C. Cavazzoni, D. Ceresoli, M. Cococcioni, N. Colonna, I. Carnimeo, A. D. Corso, S. de Gironcoli, P. Delugas, R. A. DiStasio, A. Ferretti, A. Floris, G. Fratesi, G. Fugallo, R. Gebauer, U. Gerstmann, F. Giustino, T. Gorni, J. Jia, M. Kawamura, H.-Y. Ko, A. Kokalj, E. Küçükbenli, M. Lazzeri, M. Marsili, N. Marzari, F. Mauri, N. L. Nguyen, H.-V. Nguyen, A. O. de-la Roza, L. Paulatto, S. Poncé, D. Rocca, R. Sabatini, B. Santra, M. Schlipf, A. P. Seitsonen, A. Smogunov, I. Timrov, T. Thonhauser, P. Umari, N. Vast, X. Wu, and S. Baroni, J. Phys.: Condens. Matter **29**, 465901 (2017).
[25] N. Troullier and J. L. Martins, Phys. Rev. B **43**, 1993 (1991).
[26] J. P. Perdew, K. Burke, and M. Ernzerhof, Phys. Rev. Lett. **77**, 3865 (1996).
[27] J. D. Pack and H. J. Monkhorst, Phys. Rev. B **16**, 1748 (1977).
[28] S. Poncé, E. R. Margine, C. Verdi, and F. Giustino, Comput. Phys. Commun. **209**, 116 (2016).
[29] J. M. Ziman, *Electrons and Phonons: The Theory of Transport Phenomena in Solids* (Clarendon, Oxford, 1960).
[30] M. A. Mitchell, J. Appl. Phys. **46**, 4742 (1975).
[31] J. Yamashita and S. Asano, Prog. Theor. Phys. **51**, 317 (1974).
[32] H. Sano, J. Phys. Soc. Jpn. **39**, 1268 (1975).
[33] N. W. Ashcroft and N. D. Mermin, *Solid State Physics* (Cengage Learning, New York, 1976).
[34] P. N. Trofimenkoff and J. W. Ekin, Phys. Rev. B **4**, 2392 (1971).
[35] W. E. Lawrence and J. W. Wilkins, Phys. Rev. B **6**, 4466 (1972).
[36] Z. Liu, M. Zhu, and Y. Zheng, J. Mater. Chem. C **7**, 986 (2019).